ORNL/TM-2023/3031

Preliminary Report on Compositional Specification for Printed 316SS

Peeyush Nandwana
Rangasayee Kannan
Selda Nayir
Caleb Massey
Chase Joslin
Fred List III

August 2023

M3CR-22OR0402012

DOCUMENT AVAILABILITY

Reports produced after January 1, 1996, are generally available free via OSTI.GOV.

Website www.osti.gov

Reports produced before January 1, 1996, may be purchased by members of the public from the following source:

National Technical Information Service
5285 Port Royal Road
Springfield, VA 22161
Telephone 703-605-6000 (1-800-553-6847)
TDD 703-487-4639
Fax 703-605-6900
E-mail info@ntis.gov
Website http://classic.ntis.gov/

Reports are available to US Department of Energy (DOE) employees, DOE contractors, Energy Technology Data Exchange representatives, and International Nuclear Information System representatives from the following source:

Office of Scientific and Technical Information
PO Box 62
Oak Ridge, TN 37831
Telephone 865-576-8401
Fax 865-576-5728
E-mail reports@osti.gov
Website https://www.osti.gov/

ORNL/TM-2023/3031

Advanced Materials and Manufacturing Technologies Program

PRELIMINARY REPORT ON COMPOSITIONAL SPECIFICATION FOR PRINTED 316SS

Peeyush Nandwana
Rangasayee Kannan
Selda Nayir
Caleb Massey
Chase Joslin
Fred List III

August 2023

M3CR-22OR0402012

Prepared by
OAK RIDGE NATIONAL LABORATORY
Oak Ridge, TN 37831
managed by
UT-BATTELLE LLC
for the
US DEPARTMENT OF ENERGY
under contract DE-AC05-00OR22725

CONTENTS

LIST OF FIGURES

LIST OF TABLES

ABSTRACT

The Advanced Materials and Manufacturing Technologies Program is focused on accelerating the development and deployment of advanced materials and components fabricated via additive manufacturing (AM). A key challenge for the widespread adoption of AM is the variability in material properties, which can originate from powder feedstock, process parameters, geometry, and the machine. AM powder feedstock compositions are based on those developed for conventional manufacturing. However, the smaller melt pools combined with multiple melt cycles over the course of a build can have substantial effects on the local phase selection resulting from minor batch-to-batch feedstock variability. Therefore, this report focuses on coupling CALPHAD calculations with data mining and visualization to aid the development of compositional specifications for stainless steel 316, an important alloy for nuclear applications and suitable for AM. This work reports that δ-ferrite formation has a stronger dependence on the amount of nickel in the alloy despite nickel being an austenite stabilizer. These findings show the need for exercising a tighter control on the amount of nickel in the alloy compared with the amount of chromium, which is a ferrite stabilizer.

1. INTRODUCTION

The Advanced Materials and Manufacturing Technologies (AMMT) Program aims to provide a technological solution to the current and prospective nuclear reactor fleet by optimizing the laser powder bed processing conditions of austenitic stainless steel 316 (316SS). Currently, a limited number of reactors (e.g., sodium-cooled fast reactor) use austenitic stainless steel as a structural alloy. Therefore, a rapid qualification of new additively manufactured materials, such as 316H, is necessary to accelerate their nuclear application, thereby contributing to the advancement of field.[1] For this purpose, revealing compositional variations of austenitic stainless steel is a stepping stone to produce robust materials that can withstand different types of coolants and irradiation effects.

Laser powder bed fusion (LPBF) has been identified as a key additive manufacturing (AM) technology to fabricate components for nuclear applications owing to its ability to make high-resolution near-net-shape components. However, its widespread use is limited by the variability in microstructure and material properties that can be a result of the powder feedstock,[2] process parameters,[3] geometry,[4] or the AM[5] system used. Even if a specific machine is used to print the same geometry repeatedly, the batch-to-batch variability in powder feedstock chemistry can cause a variation in material properties.[6] The powder feedstock chemistry ranges used for LPBF are based on compositions developed for conventionally processed material, such as ASTM International's ASTM A240 specification for rolled 316SS plate material.[7] The composition specifications for conventional material have been written based on the ability to achieve predictable properties within the given bounds, largely because the material is subjected to homogenization and thermomechanical treatments to obtain a homogeneous microstructure.

In the case of LPBF, the material undergoes layer-by-layer deposition and is fused by small melt pools, each of which undergoes very high cooling rates of the order of 10^5–10^6 K/s.[8] Such repeated thermal cycles result in heterogeneous hierarchical microstructures but can also enable superior properties for AM material compared with their conventionally processed counterparts. In the case of 316SS-L, a low–interstitial content variant of 316SS (carbon <0.03 wt %), LPBF results in a dislocation substructure that gives comparable strength and significantly higher elongation to failure compared with conventional 316SS-L, especially at room temperature.[9,10] At the same time, LPBF also causes significant partitioning of chromium and nickel, also called *solute partitioning*, that can potentially affect other properties such as creep and corrosion in the extreme environments experienced in nuclear applications.[11] A homogenizing heat treatment can be used to minimize the extent of solute partitioning but will also annihilate the beneficial dislocation substructures that can serve as potential defect sinks during irradiation.[12] Similarly,

for 316SS-H that contains a higher amount of carbon in the range 0.04–0.1 wt %, a direct aging heat treatment can be used to obtain a high number density of finer carbides on the dislocation structure from LPBF compared with a conventional homogenization and aging treatment. For example, in the case of grade 300 maraging steel, precipitation-strengthened material such as 316SS-H, direct aging has been shown to be beneficial.[13] Therefore, it is important to control the variables such as feedstock chemistry and process settings such that repeatable material properties are obtained in as fabricated condition for 316SS.

For a given LPBF system, powder feedstock chemistry is the first critical source of variability that is encountered during manufacturing. Even subtle variations in powder chemistry can cause significant changes in microstructure evolution and subsequent properties, mainly because of the highly localized melting that occurs repeatedly over the course of a build. Different regions even within a single melt pool can undergo different solidification pathways.[11] Solidification pathways are dependent on chemistry, as well as thermal gradients, which are a function of process variables and geometry. Although the latter can be controlled, batch-to-batch variability in powder feedstock is not only common but expected.[6] Currently, either this variability is not considered or is dealt with by varying the process parameters during fabrication until the desirable properties are achieved. Therefore, an imminent need exists to write narrower composition specifications for 316SS-L and 316SS-H for fabrication via AM.

Thermodynamic and kinetic calculations can be conducted to determine the effects of different alloying elements on the resulting phase evolution during solidification or on phase boundaries. Currently, these tools are used in a descriptive manner (i.e., once the powder feedstock chemistry is known, they are used to explain the resulting microstructures). Often, to understand the role of alloying elements, one element is varied at a time while keeping all others constant, and phase diagrams are plotted. Neither the descriptive use nor the varying an element one at a time approach is viable to develop the compositional specifications for printed 316SS. Kannan et al. developed a CALPHAD data mining and visualization approach to simultaneously vary multiple elements to determine the effects of subtle chemistry changes on δ-phase formation in 316SS-L. They explored 5,000 compositions of 316SS-L, all within the bounds of ASTM specifications, and found that there can be significant variation in the δ-phase.[14] Later, Kannan and Nandwana extended this approach to generate 1 million synthetic compositions to enable new alloy discovery.[15] This report has combined the two approaches (i.e., data mining and synthetic data generation) to understand the effects of various elements on phase evolution for 316SS-L and 316SS-H by exploring 1 million compositions, all within the ASTM specifications, to help narrow down the compositional specifications of printed 316SS for nuclear applications.

Even if the powder specification is written narrowly, it is known that certain elements with high vapor pressure are prone to selective losses during LPBF. To this effect, this research conducted builds on commercially available 316SS-L powders with varying energy densities to determine if any notable variability exists between the feedstock and part chemistry. This work found that the powder chemistries translate to build chemistry, thereby making the data mining approach a viable approach for developing compositional specifications for printed 316SS. The remainder of the report is organized to first discuss the effect of energy density on printed part chemistry as compared with feedstock chemistry. Following this, the data mining approach is presented to develop compositional specifications for the printed material.

2. CHEMISTRY: POWDER TO PART

The powder feedstock chemistry of 316SS-L powders procured from Praxair Surface Technologies Inc. are summarized in Table 1 and compared with the ASTM specifications. The specification either provides

the range for specific elements or, in the case of a single number, provides the upper bound. The powders had a nominal size distribution of 15–45 µm.

Table 1. The ASTM specifications for 316SS-L powders and the measured feedstock chemistry for the powders used in this study. The compositions are in weight percent.

	Fe	C	Mn	Si	Cr	Ni	Mo	S	N	P	O	Al
ASTM[7]	Bal.	0.03	2	0.75	16–18	10–14	2–3	0.03	0.1	0.045	—	—
Powder	Bal.	<0.005	1.1	0.48	16.86	12.07	2.5	0.005	0.006	0.005	0.056	0

Note: The amount of iron is the balance once the weight % of all other elements are added such that the total is 100%.

The powders were used to make a specific geometry, as shown in Figure 1a, with various features such as fins, flat regions, and cylindrical posts to evaluate the cross section effects on resulting microstructure evolution.[16] A General Electric (GE) Concept Laser M2 system was used to deposit multiple coupons with different combinations of laser power, velocity, and hatch spacing to vary the energy input during printing. The layer thickness was kept constant at 50 µm, and Figure 1b shows the deposited parts.

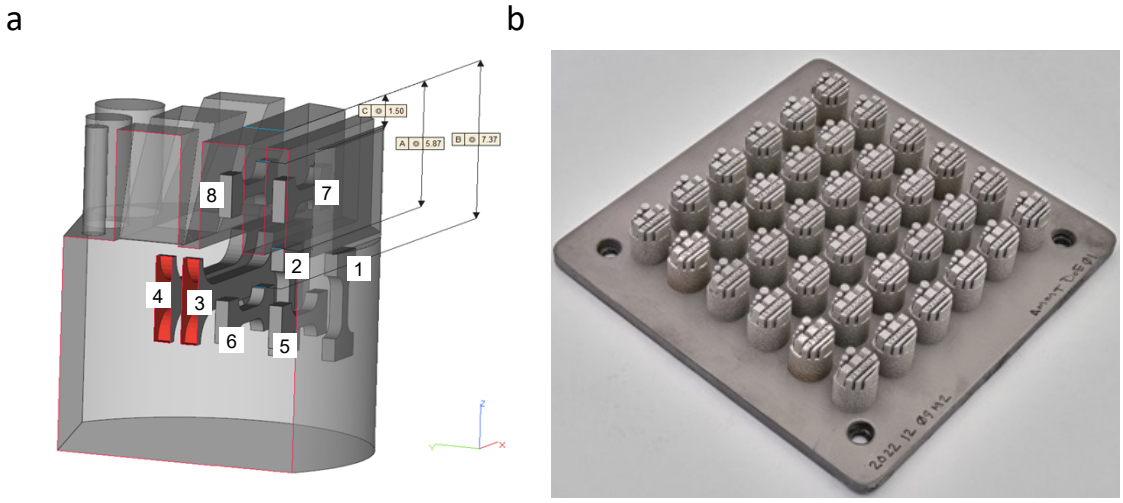

Figure 1. (a) Schematic of the analysis coupon, and (b) coupons deposited using different process settings.

The energy input during deposition of each coupon was rationalized by using the volumetric energy density (E_d), defined as

$$E_d = \frac{P}{v \times h \times t}, \#(1)$$

where P is the laser powder, v is the beam velocity, h is the hatch spacing, and t is the layer thickness. Builds were deposited within a wide span of energy densities ranging from 14 to 135 J/mm^3. Lack of fusion porosity was common at energy density values less than 39 J/mm^3, and samples below this threshold were not chosen for analysis. The chemical composition of 316SS-L powder and builds was analyzed with inductively coupled plasma mass spectrometry, and the carbon and sulfur contents were determined with LECO combustion in compliance with ASTM E1019. The content of hydrogen, oxygen, and nitrogen were analyzed with inert gas fusion at Dirats Laboratories. The compositions for selected samples as a function of energy density are shown in Table 2.

Table 2. The composition of selected builds as a function of energy density (ED). The compositions are in weight percent.

ED (J/mm^3)	C	Cr	Ni	Mn	Mo	Si	P	S	N	O	Cu	Co
39	0.003	16.88	11.87	1.03	2.51	0.4	0.007	0.004	0.007	0.051	0.15	0.05
43	0.002	16.74	12.26	1.02	2.5	0.45	0.007	0.004	0.007	0.05	0.09	0.05
51	0.002	16.75	12.05	1.01	2.52	0.47	0.009	0.004	0.006	0.05	0.27	0.05
52	0.002	16.85	11.88	1.01	2.52	0.16	0.008	0.003	0.007	0.047	0.27	0.05
71	0.002	16.86	11.64	0.97	2.5	0.43	0.007	0.004	0.007	0.046	0.2	0.05
81	0.002	17	11.53	1.03	2.55	0.48	0.009	0.004	0.006	0.048	0.09	0.05
135	0.002	16.91	11.58	0.99	2.51	0.45	0.007	0.004	0.006	0.047	0.14	0.05

All the elements are within the specification range, and there does not appear to be a noticeable change in the composition of individual elements with energy density or when compared with the powder feedstock composition (refer to Table 1). In the deposited builds, chromium varies between 16.74 and 17.00 wt %, nickel varies from 11.53 to 12.26 wt %, manganese varies from 0.97 to 1.03 wt %, molybdenum varies from 2.5 to 2.55 wt %, and silicon varies from 0.16 to 0.48 wt %. Although the variation in silicon seems rather large, notably, only one sample resulted in silicon content of 0.16 wt %, whereas most measurements were between 0.4 and 0.48 wt %. On the other hand, the interstitials such as carbon, nitrogen, and oxygen do not seem to have any notable variation, and the same observation holds true for the minority elements such as copper and cobalt. To determine if there is any systematic dependence of composition variations on energy density, the data for select elements were plotted, as shown in Figure 2.

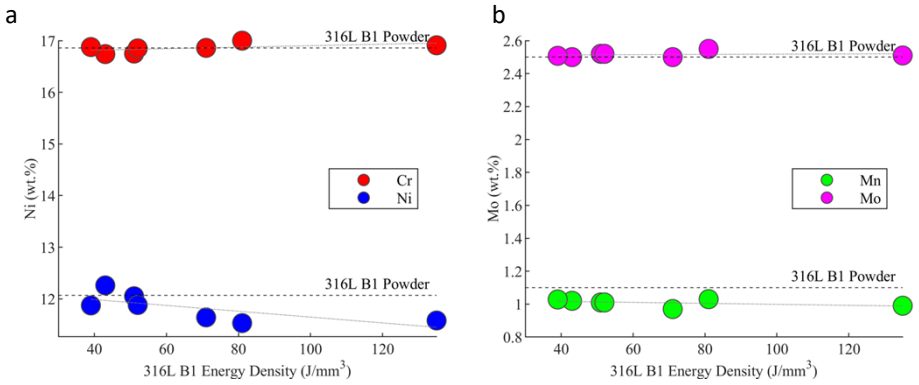

Figure 2. (a) Chromium and nickel and (b) manganese and molybdenum as a function of energy density. The dotted horizontal lines show the same element compositions in the powder feedstock.

No correlation seems to exist between chromium and molybdenum regarding energy density. However, increasing energy density results in an approximately 0.5% reduction in nickel content in the builds as compared with the powder feedstock. Similarly, a small but correlative drop exists in manganese with increasing energy density. Furthermore, samples were down-selected to determine the effect of energy density and, consequently, the subtle chemistry changes on tensile strength and microstructure, and the results are summarized in Figure 3. The tensile samples were extracted from the bulk region of the test coupon shown in Figure 1a. The tensile strength and total elongation were similar for all the conditions. The detailed texture and grain size analysis showed that 316SS-L was composed of randomly oriented smaller grains (~20 μm), and their size, morphology, and texture does not appear to have a strong dependence on energy density. Even though the tensile strength and the grain structure appear to be

insensitive to energy density, notably, the changing process variables can have a significant effect on solute partitioning. The effects of process variables on solute partitioning and dislocation cell structures are beyond the scope of this report and are under investigation.

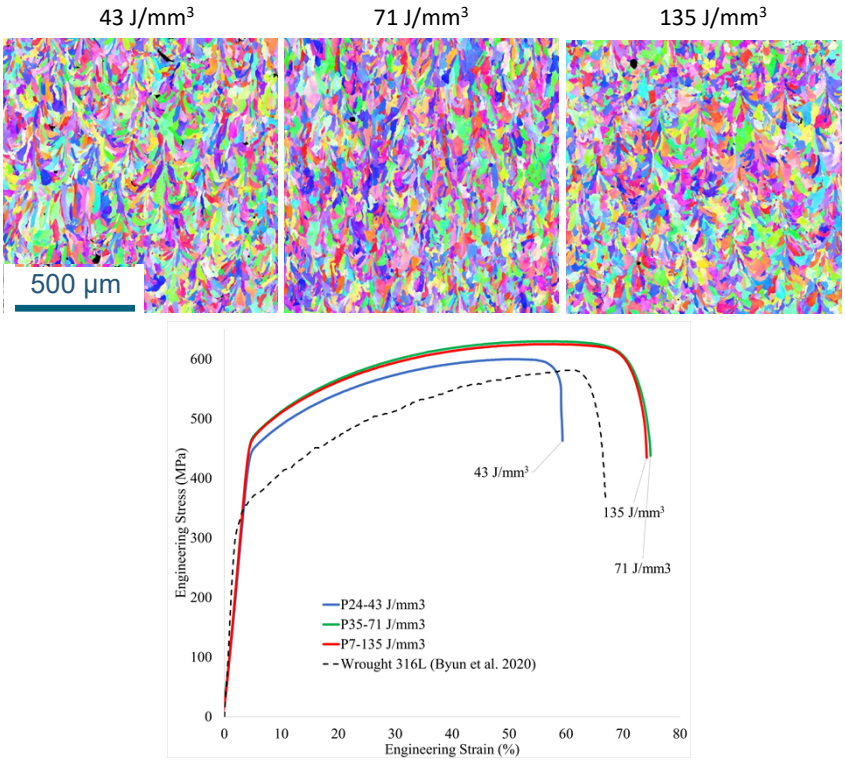

Figure 3. The tensile strength and inverse pole figure maps for selected samples. The wrought 316SS-L stress strain plot, shown with dashed lines, was reproduced from Byun et al.[17]

This discussion highlights that the powder feedstock chemistry translates to the chemistry of printed 316SS coupons over a wide range of process parameters. The relative insensitivity of printed coupon chemistry on process variables is promising because it enables the development of narrower powder feedstock specifications suitable for printed 316SS-L and 316SS-H.

3. CALPHAD AND DATA MINING FOR COMPOSITIONAL SPECIFICATIONS

316SS-L usually solidifies in an austenitic microstructure. However, recent work has shown that depending on the solidification conditions, the solidification can either occur directly via the austenitic phase field or could proceed via an austenitic–ferritic phase field, which eventually transforms to austenite at room temperature.[11] However, if the cooling rates are too fast, the δ-ferrite can be retained even at room temperature and can negatively affect the fracture toughness and corrosion resistance.[18,19] Therefore, a powder composition specification aimed at minimizing the δ-phase formation at the end of solidification would be critical to avoid the possibility of any retained δ-ferrite at room temperature. To determine a compositional specification for 316SS-L, 1,000 compositions were chosen, all of which were within the ASTM specifications shown in Table 1. A Gaussian distribution was used for all the elements, with the tails ending in the minimum and maximum allowable limits as shown in Figure 4. This distribution is a reasonable assumption because an atomization run is more likely to follow a Gaussian distribution around the average range for each element. Cr_{eq} = Cr + Mo + 1.5Si + 0.5Nb and Ni_{eq} = Ni + 0.5Mn + 30C + 30N were used to rationalize the effects of elemental variations on eventual

phase evolution because Cr_{eq} and Ni_{eq} account for ferrite stabilizing and austenite stabilizing effects of the constituent elements.[14] Once the compositions were generated, the TC-Python module of ThermoCalc was used to generate phase diagrams and extract data such as equilibrium phases while Scheil simulations were conducted to determine the phase fractions during solidification.

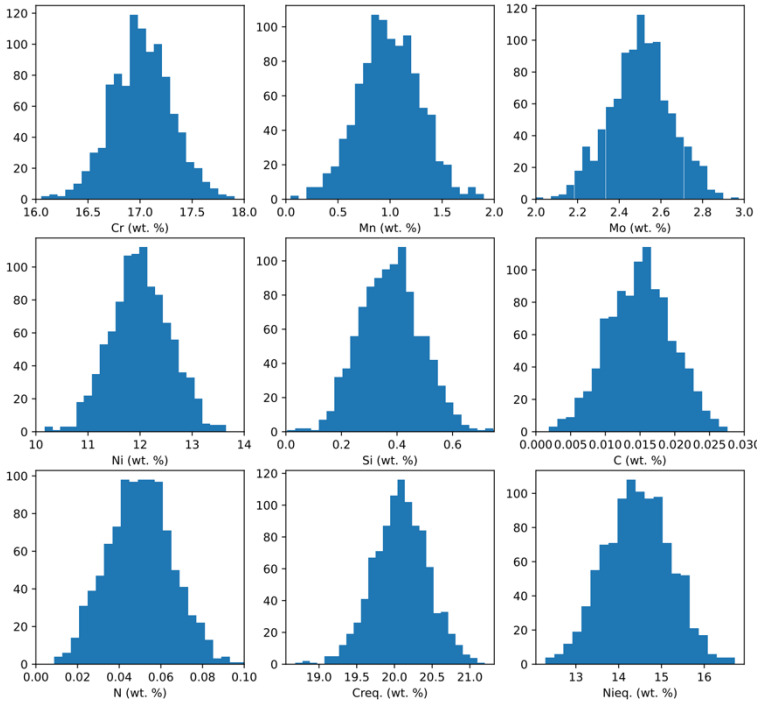

Figure 4. The Gaussian distribution of different elements in 316SS-L, along with Cr_{eq} and Ni_{eq} distribution.

The relevant data was extracted from the TC-Python calculations, following which a Gaussian Copula machine learning model was used to learn from the input data (i.e., data from thermokinetic calculations on the 1,000 compositions). Following this step, a Fast_ML synthetic data generator was used to generate 1 million synthetic compositions, all within ASTM specifications. The reason for generating synthetic compositions was to increase the evaluated composition space and therefore increase the reliability of the resulting trends. The trained Gaussian Copula model was then used to extract the relevant phase information for the 1 million compositions. The relevant data, such as Cr_{eq}, Ni_{eq}, equilibrium δ-phase fraction, and δ-phase fraction at the end of solidification using the Scheil simulation, was visualized using parallel coordinate plots. This view allows the trends to be visualized intuitively and allows for selecting a desired output phase fraction; it also shows the respective composition ranges that enable the selected output. Figure 5 shows all the composition ranges that result in <15 vol % δ-phase fraction under equilibrium conditions. Figure 5 also shows that a narrower spread in Ni_{eq} is needed to obtain the desired δ-phase fraction compared with the spread in Cr_{eq}. This result is interesting because Cr_{eq} is an indicator of δ-phase stability. Therefore, it should have a stronger effect and, thus, narrower spread for the selected δ-value. Based on the parallel coordinate plot in Figure 5, the composition range for 316SS-L is recommended in Table 3.

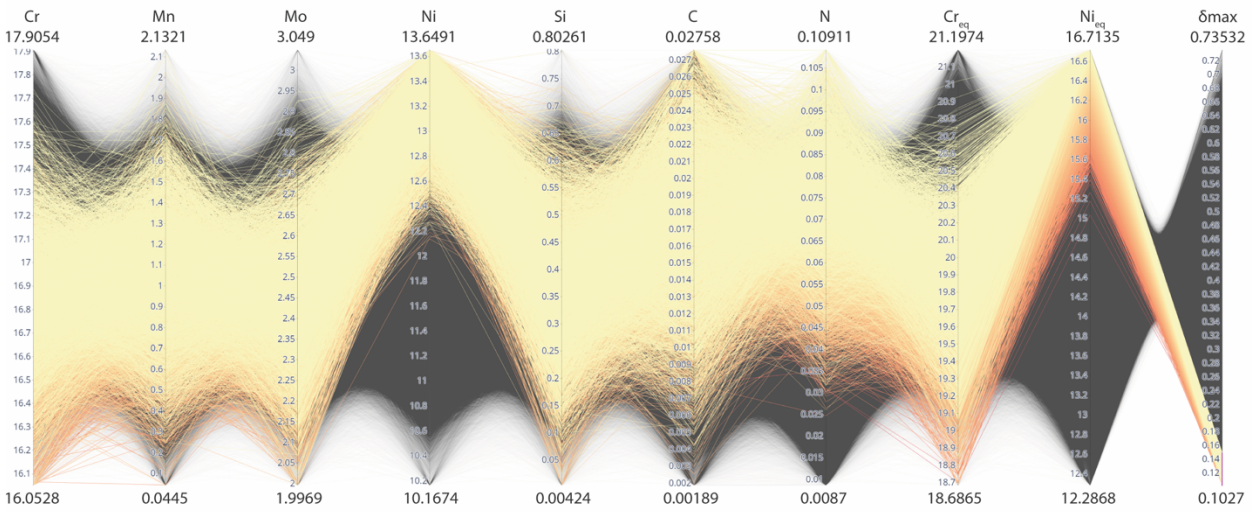

Figure 5. The parallel coordinate plot showing the compositions that result in <15 vol % δ-ferrite. The gray regions show compositions that result in δ-ferrite higher than the selected threshold level.

Table 3. The proposed composition specification for 316SS-L. The single values are the maximum allowable values. All values are in weight percent.

Fe	C	Mn	Si	Cr	Ni	Mo	N
Bal.	0.02	2.0	0.75	16–17.5	12.5–14	2–3	0.025–0.109

A similar approach as that described previously was used for 316SS-H, and the parallel coordinate plot is shown in Figure 6. In the case of 316SS-H, because the strengthening results from $M_{23}C_6$ carbides, the parallel coordinate plots and, subsequently, the compositions were identified to maximize the carbides (>1.6 vol %) while keeping δ-ferrite low (<15 vol %). Similar to 316SS-L, δ-ferrite has a stronger sensitivity to Ni_{eq} compared with Cr_{eq}, as evidenced by a broader spread for chromium and Cr_{eq} compared with nickel and Ni_{eq} values in the plot.

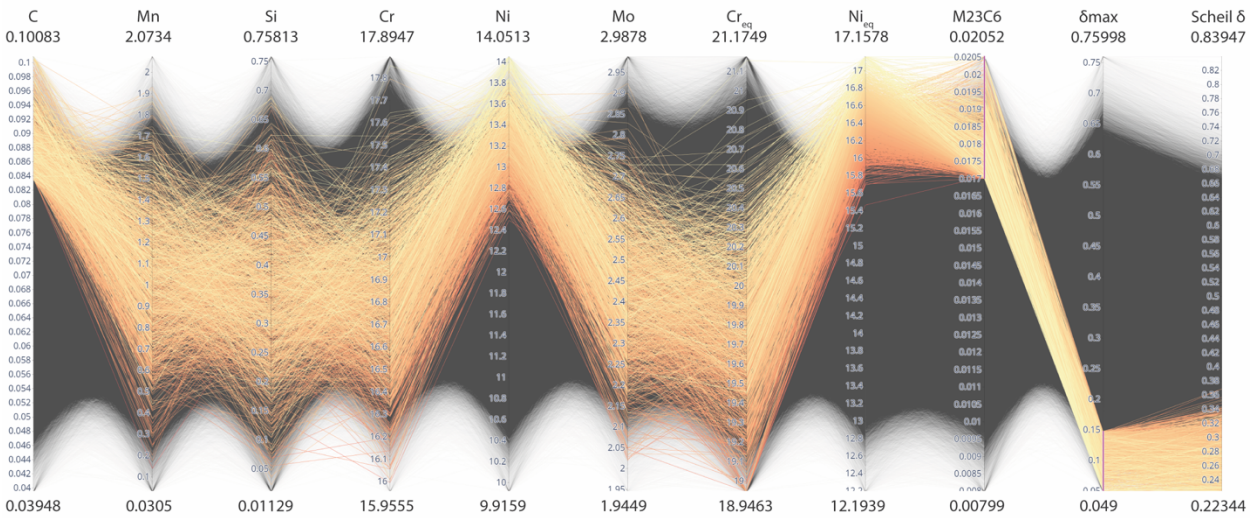

Figure 6. The compositions that enable maximizing carbides (>1.7 vol %) while minimizing δ-ferrite (<15 vol %). The grey regions show compositions that result in $M_{23}C_6$ lower and δ-ferrite higher than the selected threshold level.

The proposed composition range for 316SS-H powders is shown in Table 4 and compared with the current specification.

Table 4. Comparison of the ASTM specifications with the proposed compositions for 316SS-H. The single values are the maximum allowable values. All values are in weight percent.

	Fe	C	Mn	Si	Cr	Ni	Mo
ASTM [5]	Bal.	0.04-0.1	2.0	0.75	16-18	10-14	2-3
Proposed	Bal.	0.08-0.1	2.0	0.75	16-18	12-14	2-3

Interestingly, for both 316SS-L and 316SS-H, the parallel coordinate plots showed higher sensitivity to Ni_{eq} and, consequently, the amount of nickel. This result is reflected in the preliminary composition specifications, where higher amounts of nickel compared with the ASTM range are proposed (i.e., 12–14 wt % compared with 10–14 wt %), whereas the chromium range remained unchanged despite chromium being a ferrite stabilizer. This result highlights the importance of the data mining and visualization approach because based on existing knowledge and intuition, one would expect a reduction in chromium as the critical factor to minimize the δ-fraction instead of increasing the amount of nickel while keeping chromium constant.

4. CONCLUSIONS

This report summarizes the use of thermokinetic calculations coupled with machine learning models to propose a narrower compositional specification for printed 316SS. The use of this data visualization approach revealed interesting insights about the sensitivity of relevant phases on different constituent elements of 316SS (i.e., nickel having a stronger influence on controlling the δ-ferrite phase fraction rather than chromium, which is a ferrite stabilizer). Although the composition specifications can be written for the powder feedstock, it can be useful only if the feedstock composition translates to the printed material composition. To this effect, this study printed 316SS-L samples over a wide range of process settings and measured the compositions. The findings indicate that the powder compositions

translate reasonably well to printed material compositions and results in comparable microstructure and properties. Therefore, the use of the proposed approach in this material can be used to reduce the feedstock-related variability, as well as designing AM feedstock to influence the as-fabricated microstructures and properties.

5. REFERENCES

1. *Advanced Materials and Manufacturing Technologies (AMMT) 2022 Roadmap*.
2. Clayton, J., D. Millington-Smith, and B. Armstrong. 2015. "The Application of Powder Rheology in Additive Manufacturing." *JOM* 67: 544–548.
3. Wang, Z. et al. 2020. "Uncertainty quantification and reduction in metal additive manufacturing." *NPJ Comput Mater* 6, no. 175.
4. Nandwana, P., A. Plotkowski, R. Kannan, S. Yoder, and R. Dehoff. 2020. "Predicting geometric influences in metal additive manufacturing." *Mater Today Commun* 25, no. 101174.
5. Ituarte, I. F., E. Coatanea, M. Salmi, J. Tuomi, and J. Partanen. 2015. "Additive Manufacturing in Production: A Study Case Applying Technical Requirements." *Phys Procedia* 78: 357–366.
6. Voisin, T. et al. 2021. "New insights on cellular structures strengthening mechanisms and thermal stability of an austenitic stainless steel fabricated by laser powder-bed-fusion." *Acta Mater* 203, no. 116476.
7. ASTM International. 2004. *Standard Specification for Chromium and Chromium-Nickel Stainless Steel Plate, Sheet, and Strip for Pressure Vessels and for General Applications*. ASTM A240/A240 M-22. DOI: 10.1520/A0240_A0240M-22.
8. Hooper, P. A. 2018. "Melt pool temperature and cooling rates in laser powder bed fusion." *Addit Manuf* 22: 548–559.
9. Wang, Y. M. et al. 2018. "Additively manufactured hierarchical stainless steels with high strength and ductility." *Nat Mater* 17: 63–70.
10. Dryepondt, S., P. Nandwana, P. Fernandez-Zelaia, and F. List. 2021. "Microstructure and high temperature tensile properties of 316L fabricated by laser powder-bed fusion." *Addit Manuf* 37, no. 101723.
11. Godfrey, A. J. et al. 2022. "Heterogeneity and Solidification Pathways in Additively Manufactured 316L Stainless Steels." *Metall Mater Trans A Phys Metall Mater Sci* 53: 3321–3340.
12. Li, S. et al. 2020. "Evolution of cellular dislocation structures and defects in additively manufactured austenitic stainless steel under ion irradiation." *Scr Mater* 178: 245–250.
13. Nandwana, P., R. Kannan, and D. N. Leonard. 2020. "Leveraging Solute Segregation in Laser Powder Bed Fusion to Achieve Superior Strength and Ductility Via Single-Step Heat Treatment in Ti-Free Grade 300 Maraging Steel." *JOM* 72: 4221–4231.
14. Kannan, R. et al. 2022. "Data Mining and Visualization of High-Dimensional ICME Data for Additive Manufacturing." *Integr Mater Manuf Innov* 11: 57–70.
15. Kannan, R. and P. Nandwana. 2023. "Accelerated alloy discovery using synthetic data generation and data mining." *Scr Mater* 228.
16. Ziabari, A. et al. 2023. "Enabling rapid X-ray CT characterisation for additive manufacturing using CAD models and deep learning-based reconstruction." *NPJ Comput Mater* 9, 91.
17. Byun, T. S. et al. 2020. *Mechanical Properties and Deformation Behavior of Additively Manufactured 316L Stainless Steel-FY 2020*. ORNL/TM-2020/1574. Oak Ridge, Tennessee: Oak Ridge National Laboratory.
18. Sun, Z., X. Tan, S. Beng Tor, and W. Yee Yeong. 2016. "Selective laser melting of stainless steel 316L with low porosity and high build rates." *Materials and Design* 104: 197–204. DOI: 10.1016/j.matdes.2016.05.035.
19. Sarafan, S. et al. 2022. "Benchmarking of 316L Stainless Steel Manufactured by a Hybrid Additive/Subtractive Technology." *Journal of Manufacturing and Materials Processing* 6, no. 30.